Selective Passivation of 2D MoS2 Nanosheets Surface Defects by Spontaneous Growth of Au Nanoparticles for Full Response-Recovery NO2 Detection at Room Temperature

Pingping Ni, Elmehdi Ould Maina, Kassiogé Dembélé, Diana Dragoe, Fatima Zahra Bouanis, Abderrahim Yassar

Selective Passivation of 2D MoS_2 Nanosheets Surface Defects by Spontaneous Growth of Au Nanoparticles for Full Response-Recovery NO_2 Detection at Room Temperature

Pingping Ni[1,2], Elmehdi Ould Maina[1,2], Kassiogé Dembélé[1,3], Diana Dragoe[4], Fatima Zahra Bouanis[1,2], Abderrahim Yassar[1]

[1]LPICM, CNRS, Ecole Polytechnique, Institut Polytechnique de Paris, 91128, Palaiseau, France ; pingping.ni@polytechnique.edu; elmehdi.ould-maina@polytechnique.edu; abderrahim.yassar@polytechnique.edu;

[2]COSYS-IMSE, Univ. Gustave Eiffel, F-77454 Marne-la-Vallée, France ; fatima.bouanis@univ-eiffel.fr

[3]Centre interdisciplinaire de microscopie électronique, Ecole Polytechnique, 91120 Palaiseau, France ; kassioge.dembele@polytechnique.edu

[4]Université Paris-Saclay, ICMMO, UMR 8182 CNRS, 91405 Orsay, France ; diana.dragoe@universite-paris-saclay.fr

*Correspondence: fatima.bouanis@univ-eiffel.fr; abderrahim.yassar@polytechnique.edu

Abstract

Full recovery at RT is quite challenging for two dimensional transition metal dichalcogenides chemiresistive gas sensors. The main reason for the incomplete recovery is the strong bonding of gas molecules onto sensing layer defects. Here, we show that the recovery rate of MoS_2 chemiresistive NO_2 sensors can be improved by selective passivation of MoS_2 nanosheets (NSs) defects with Au nanoparticles (NPs) via a simple spontaneous reduction method. MoS_2 NSs were produced by liquid shear exfoliation. Pristine and Au NPs functionalized MoS_2 were characterized using ς-potential, UV-Visible spectroscopy, TEM, SEM, AFM, EDS, XRD, XPS and Raman spectroscopy. The analyses confirm the presence of Au NPs on the edges of MoS_2 NSs at defective sites with NP sizes of 1-4 nm and 5-30 nm. Both pristine MoS_2 and Au-decorated MoS_2 NSs were employed to fabricate NO_2 chemiresistive devices. Au-decorated MoS_2 sensors showed an improved performance (for 1 ppm NO_2, Au-MoS_2 sensor exhibited a response of 5.6% instead of 2.2% for MoS_2 sensor), and gave faster response and better recovery time. Concurrently, the functionalization is independent of the adsorption and desorption of NO_2. Most importantly, the functionalization of MoS_2 NSs helps to full response-recovery within one hour, without either thermal or UV irradiation treatment.

Keywords: 2D-TMDs materials, chemiresistive gas sensor, noble metal nanoparticles, surface functionalization, solution processing, defect engineering, NO_2 sensing

1. Introduction

Recent years have witnessed the emergence of two-dimensional (2D) transition metal dichalcogenides (TMDs) as a promising platform for fabricating a wide range of electronic devices for various applications. From a fundamental point of view, they have also been explored for their rich low-dimensional physics.

However, despite their successful application in many areas and impressive performance, processingthese materials remains a challenge for the future industrial-scale applications. Solution-processed methods offer a promising approach for manufacturing low-cost, printable devices and photocatalyst based on 2D-materials for environmental and energy applications.[1,2,3] Liquid-phase exfoliation (LPE) of 3D bulk crystals into their 2D analogues, offers a way to overcome these challenges[2,4] and represents a promising way to produce nanosheets (NSs) for various large-scale applications. Simple exfoliation method combined with large-scale production of atomically thin TMDs NSs make solution-processed TMDs thin films one of the best strategy for the fabrication of wearable optoelectronic devices. .

However, solution-processed 2D TMDs materials produces NSs with a high defect content, which may hinder their use for optoelectronic applications, where the high-performance capabilities are required. Concurrently, these defects are considered as an attractive alternative to alter their physicochemical and catalytic properties.[5] Thus , understanding and engineering defects in TMDs NSs is a key to rationally design superior 2D-materials.[6] Various strategies have thus been employed to control defect engineering in TMDs materials, with an aim to tune their structural, electronic, optical, and catalytic properties.[7] To this end, surface functionalization of TMDs NSs has been proven to be an effective way to passivate their surface and to control their reactivity, which are essential for many applications.

~~As in a typical example, in a chemiresistive gas sensor the mechanism by which the target gas molecules interact with sensing layer can involve either covalent or non-covalent bonding: chemisorption or physisorption processes, depending on the chemical structure of the sensing materials.~~

For example, in chemiresistive gas sensors, the interaction between target gas molecules and the sensing layer may involve either covalent or non-covalent bonding—known as chemisorption or physisorption—depending on the chemical structure of the sensing materials. Previous studies have shown that for pristine TMDs, gas molecules interact with sensing materials primarily through physisorption process, while chemisorption is more predominant on defective TMD sensing layers or at defect sites.[9] The physisorption process is characterized by a weak adsorption energy and a significant distance between the gas molecules and the TMD film. Moreover, there is minimal charge transfer between the gas molecules and the TMD film, resulting in an almost unchanged electronic structure. As a result, gas sensors employing pristine TMD films show fast recovery but lower sensitivity. Chemisorption, on the other hand, involves chemical bonding between gas molecules and sensing layer, with a high interaction energy and slow recovery time. Besides, in the case of the chemisorption process, a baseline drift is often observed which results from the incomplete desorption.[10]

One way to enhance the recovery properties of 2D TMD gas sensors, is to functionalize their surface by a specific group or to hybridize them with other functional materials. Of all surface functionalization methods, incorporating noble metal nanoparticles (NPs) on the surface of 2D material NSs has proven to be an effective way to enhance gas sensing performance.[11, 12] For instance, Zhou et al. have shown that Au NPs-functionalized MoS_2 NSs possessed remarkable response to NO_2 at room temperature (RT) under the exposure to the UV light.[13] The Au NPs-decorated MoS_2 sensor demonstrated a sensibility of 10% in the dark to 2.5 ppm NO_2, which is 2-fold of the response of bare MoS_2 sensor. This improvement is attributed to the produced interfaces and spillover effect introduced by Au NPs to generate more reaction sites, and the reduction of resistance baseline after Au functionalization.

Rahman et al. successfully applied Au NPs-decorated MoS_2 NSs as a sensing layer for RT detection of N_2O gas.[14] The functionalized sensor exhibited high sensitivity and a better response of 58% improvement over the bare MoS_2 sensors, due to the n-doping effect of Au NPs. Using the localized surface plasmon resonance effect, Hu et al designed a visible light assisted NO_2 gas sensor using Au NPs-decorated MoS_2.[15] The response to NO_2 was tested and the results demonstrated that the Au-decorated MoS_2 sensor exhibited an outstanding improvement in NO_2 sensing compared to bare MoS_2 sensor, and was able to detect NO_2 gas down to ppb-level with enhanced sensitivity, complete recovery, reliable stability and selectivity. The development in sensing performance is believed due to the electronic and chemical sensitization produced by the interfacial contact of Au-MoS_2 hetero-interface.

Rawat et al. [16] constructed a gas sensing device by employing an inert gas evaporation method to graft Au NPs of different sizes onto MoS_2 nanoflowers, the decorated sensor showed a response of 69% to NH_3 and a response of 79 % to CO, which are 5 and 3.5 times better than the responses of bare MoS_2 sensor to CO and NH_3, respectively. According to the results of x-ray photoelectron spectroscopy (XPS) and ultraviolet photoelectron spectroscopy analysis, it is proven that a Schottky barrier is formed due to the improved interfacial interaction between MoS_2 and Au NPs, which is responsible for the enhanced response in gas sensing.

While there is still debate in the literature regarding the exact mechanism behind how metallic NPs contribute to the enhancement of sensor response. Two mechanisms have been proposed, one involves the Schottky barrier formed between the noble metal NPs and the 2D materials, which can improve the gas sensing performance by adjusting the electrical characteristics. Second one is based on the electronic and chemical sensitization mechanisms brought by the spillover effect of the decoration of noble metal NPs, by enhancing the preabsorbed molecular oxygen, in the air via adsorption and accumulation on the surface of the NPs, so in this way the NPs act as additional active sites, strengthening the gas adsorption ability of gas sensing materials, and then enhancing their sensing performance.[17]

The incorporation of metal NPs into TMDs NSs is typically achieved through two methods: in-situ or ex-situ functionalization, this former includes spontaneous deposition. The spontaneous reduction of metal ions by TMDs is governed either by the energy gap between the metal ion reduction potential and the TMDs work function.[18] Furthermore, it has been demonstrated that the functionalization tends to occur at the edges of the NSs where the defect are present, and then at line

defects withinthe basal planes.[17,19] This functionalization method enables the formation of smaller metal NPs on NS surface with a high dispersion and homogeneous size compared with other method, providing thus an abundance of catalytically active sites for reaction.

Previous studies have shown that Au NPs-decorated MoS_2 NSs can be synthesized via spontaneous reduction of gold ions (Au^{3+}) on the surface of LPE MoS_2 NSs.[18,20] Notably, this deposition process does not require additional reduction treatments, reducing agents, or catalysts, due to the difference in the work function of MoS_2 and the reduction potential of $AuCl_4^-$. This differentiates it from traditional electroless deposition. In this process, discrete Au NPs form on the MoS_2 NSs surface thanks to the high-energy sites, especially the edges and defects on MoS_2 NSs acting as effective heterogeneous nucleation sites for anchoring of Au NPs.

, While solution processability is one of the advantages of liquid exfoliated 2D-TMDs materials, most performance solution processed 2D-TMDs sensors are fabricated using drop casting method. However thismethod is not suitable for manufacturing large area devices, and often fails to produce a continuous uniform film, due to the differential evaporation rates of solute–solvent, "coffee ring effect" and a lack of reproducibility and control of thin film thickness Therefore, developing reliable and of controllable method to fabricate thin film of monolayer or few layers of TMD NSs is in s high demanThis study explores high shear LPE of MoS_2 NSs and their further functionalization with Au NPs, via a simple spontaneous reduction method. The optical, structural, physicochemical and electrical properties of pristine and Au functionalized MoS_2 NSs were thoroughly characterized using techniques such as Raman spectroscopy, XPS, atomic force microscopy (AFM), and X-ray diffraction (XRD) which confirmed thesuccessful grafting of Au NPs onto MoS_2 NSs.

Both pristine MoS_2 and Au NPs-functionalized MoS_2 NSs were employed to fabricate chemiresistive NO_2 sensors. A vacuum-assisted filtration method was used to produce MoS_2 films which easily transferred to glass substrates. Then, 100-nm-thick patterned Au interdigitated electrodes (IDEs) were thermally deposited on MoS_2 sensing layers to produce the final chemiresistive device. The chemiresistive sensors based on MoS_2 NSs were exposed to NO_2 gas with concentrations varying from 1 to 3 ppm. Au NPs-decorated MoS_2 sensors exhibited an enhanced sensing response of 8 % to 3 ppm NO_2, more than twice compared to that of pristine MoS_2 sensors, 3.8 %. Response and recovery time analysis in 1 to 3 ppm of NO_2 concentration for both sensors showed that Au-MoS_2 sensor gives faster response and better recovery time than pristine MoS_2 devices.

2. Materials and Methods

2.1 Synthesis of MoS_2 NSs and thin film

Colloidal solutions of few-layer MoS_2 NSs were prepared using a high shear LPE method (experimental details see SI **Materials and Methods MoS_2 dispersion preparation**). Then, the exfoliated MoS_2 NSs were purified by centrifugation at 1500 rpm for two hours to remove the un-exfoliated MoS_2 flakes, the supernatant was collected for thin film fabrication. MoS_2 thin film was fabricated via vacuum-assisted filtration onto a nitrocellulose membrane and then transferred on glass by dissolving the membrane in acetone (experimental details see SI **Materials and Methods MoS_2 based thin film fabrication**).

2. 2 Functionalization of MoS_2 NSs with Au NPs

Two methods have been employed to functionalize the NSs surface with Au NPs, in solution and thin film. **In solution**, Au NPs decorating the surface of MoS_2 NSs was performed following a slightly modified spontaneous reduction method.[18] A fresh dispersion of the as-prepared MoS_2 NSs (concentration of 1.6 mg/mL determined by UV-Visible spectroscopy) was prepared as described in our previous report [21]. To avoid the redox effect of the surfactant sodium cholate (SC), which may participate to the reduction of $AuCl_4^-$ to Au^0 [22], we prepared a surfactant-free solution by re-dispersing MoS_2 NSs in deionized (DI) water, through solvent exchange method. Typically, MoS_2 aqueous dispersion (1.6 mg/mL) was subjected to centrifugation of 9500 rpm, and the sediment was collected and dispersed in DI water. The centrifugation process was repeated for three times, and then the surfactant-free MoS_2 dispersion in DI water was obtained. A certain volume of MoS_2 dispersion was mixed with $HAuCl_4$ aqueous solution (1 mg/ml) under a molar ratio between MoS_2 and Au NPs of 2:1 and sonicated for 15 mins at RT. Then the mixture was centrifuged at 9500 rpm for 30 mins, the sediment was collected and

washed 3 times with DI water to remove the unreacted $HAuCl_4$, the washed MoS_2 sediment decorated with Au NPs was re-dispersed in DI water for further characterizations (UV-Vis, Raman spectroscopy, XRD, TEM). **MoS_2 NSs thin film functionalized with Au NPs**: MoS_2 NSs thin film was prepared by a simple vacuum-assisted filtration method and transferred onto a glass substrate [21], then the functionalization with Au NPs was carried out by a simple dip-coating method of as-prepared MoS_2 NSs thin film into 10 ml solution of $HAuCl_4$ in isopropanol (1 mg/ml) for overnight. After dipping, the functionalized MoS_2 NSs thin films were washed thoroughly with DI water and isopropanol to remove the unreacted $HAuCl_4$, prepared for further gas sensing measurements.

2.3 *MoS_2-based sensor design and fabrication*

For the electrical and gas sensing measurements, IDEs with 1 mm interspacing and a width of interdigitated electrodes of 0.2 mm were deposited by thermal evaporation of 100 nm of Au on the top of 200 nm thick sensing layers. The design of IDEs mask is displayed in Figure 1 (a). Any residual solvent molecules were removed from the sensing layer surface by annealing the fabricated sensors at 100 °C in N_2 for 2 hours at ambient pressure, which were then stored in a glove box prior to gas sensing measurements.

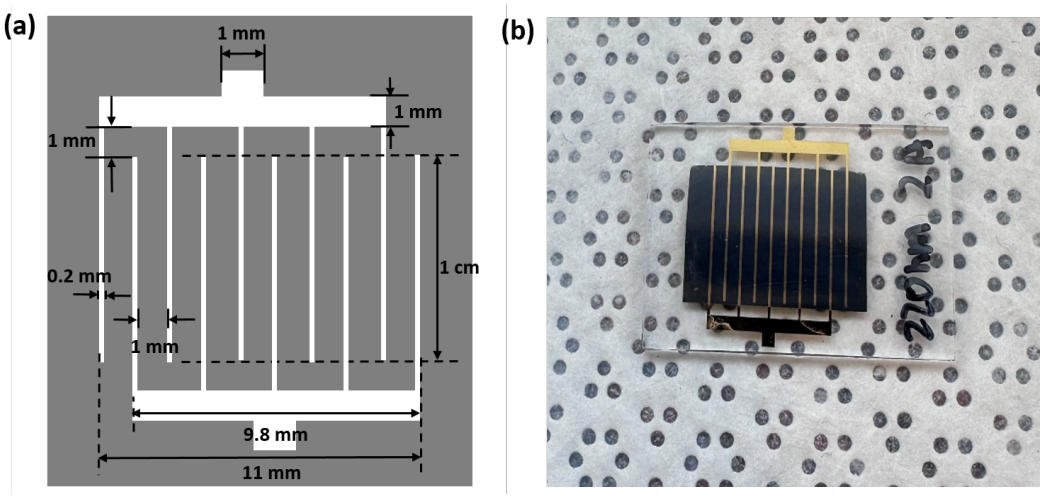

Figure 1. (a) Design of interdigitated electrodes; (b) Au-MoS_2 thin film sensor.

3. Results and Discussion

3.1 Functionalization of MoS_2 NSs with Au NPs

The MoS_2 NSs dispersion was prepared by high shear exfoliation in an aqueous solution of SC, followed by sequential centrifugation steps at different g force, and then purified by a high speed centrifugation at 9500 rpm to remove the SC. The purified MoS_2 NSs sediment was collected and re-dispersed in DI water. Figure 2 illustrates the mechanism of grafting of Au NPs on the MoS_2 NSs through electron transfer from MoS_2 NSs to the tetrachloroaurate ions. When mixing a solution of $HAuCl_4$ and MoS_2 NSs dispersion, the energy level alignment of MoS_2 with the electrochemical reduction potentials of $AuCl_4^-$ allows a spontaneous electron transfer, through a fast redox reaction between $AuCl_4^-$ and MoS_2 NSs which is evident from the change of color of the dispersion. Thus, both in-plane defects and edge sites on MoS_2 NSs provide locations with higher potential energy, making them active sites for the nucleation and growth of Au NPs.[20] These high-energy sites reduce the energy barrier for nucleation, allowing Au atoms to growth more easily and form NPs, which leads to covalently growth of Au NPs on the MoS_2 NSs surface, without the need of any additional reducing agent. Understanding this mechanism is crucial for controlling the size, distribution, and properties of Au NPs-decorated MoS_2 in various applications, including catalysis, electronics, and sensing. The electron transfer from MoS_2 to the $AuCl_4^-$ ion occurs spontaneously due to the difference of electrochemical reduction potential of $AuCl_4^-$ and the work function of MoS_2. In fact, the work function of MoS_2 varies from 5.2 eV to 5.4 eV depending on the number of layers of MoS_2 NSs [23], a value higher than that of

the electrochemical reduction potential of $AuCl_4^-$ (+1.002 V vs the standard hydrogen electrode (SHE)), allowing thus an easy electron transfer from MoS_2 to $AuCl_4^-$ ions and leading to the growth of Au NPs.

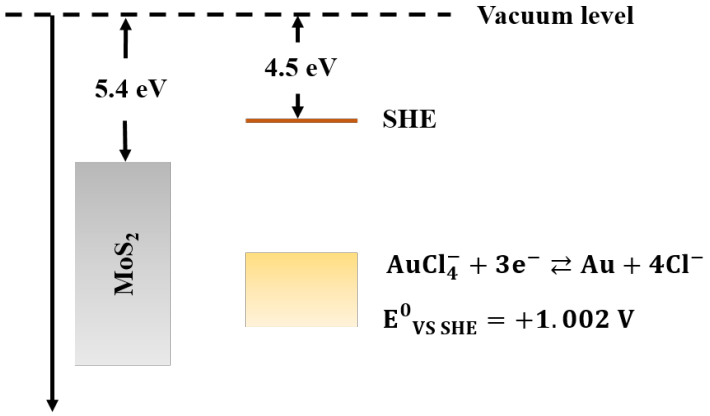

Figure 2. Energy diagram displaying the work function of MoS_2 and the reduction potential of Au^{3+} (+1.002 V versus SHE) reproduced from reference [24].

3.2 Physicochemical characterizations of Au-MoS_2 NSs dispersion

3.2.1 Optical property study

The growth process of Au NPs on MoS_2 NSs was followed by UV–Visible spectroscopy. Figure 3 displays UV-Vis. spectra of pristine MoS_2, Au NPs and Au NPs-decorated MoS_2. The peaks at around 607 nm and 667 nm, are originated from excitonic peaks of few-layer NSs of the 2H phase of the MoS_2. A plasmonic band appears at around 545 nm in the exfoliated MoS_2 dispersion upon the addition of $HAuCl_4$ solution, which indicates the formation of Au NPs in the MoS_2 NSs dispersion [25]. The reaction occurred and finished quickly since the color of the dispersion changed from green to greenish grey within several minutes (Figure 3 inset).

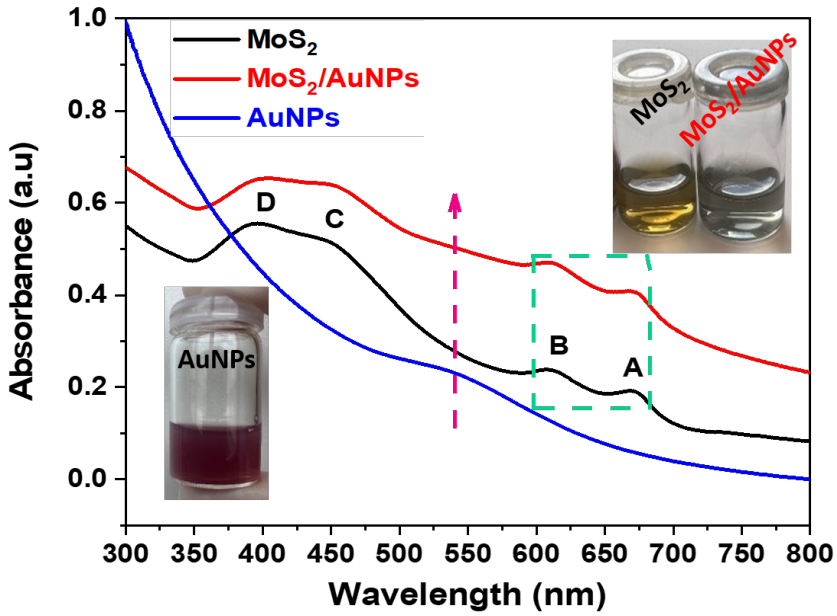

Figure 3. UV-Visible absorption spectra of 2H-MoS_2 NSs, Au NPs, and Au NPs-MoS_2 dispersions.

3.2.2 Zeta potential measurement

The changes in the surface charge of the pristine and Au NPs functionalized MoS_2 NSs were determined from zeta potential measurements of their aqueous dispersions. High value of the zeta potential indicates the stability of NPs against aggregation in the dispersion solution. We evaluated the zeta potentials of MoS_2 dispersion before and after functionalization with Au NPs (Figure 4 (a) and (b)).

The zeta potential values of MoS_2 dispersion and Au-decorated MoS_2 dispersion were measured to be -24 mV and -18.7 mV, respectively. Both MoS_2 and Au NPs-decorated MoS_2 NSs are negatively charged. However, the MoS_2 NSs were well dispersed in water, the zeta potential of MoS_2 NSs decreased after functionalization with Au NPs, meaning that the Au-MoS_2 dispersion becomes less stable than original MoS_2 dispersion.

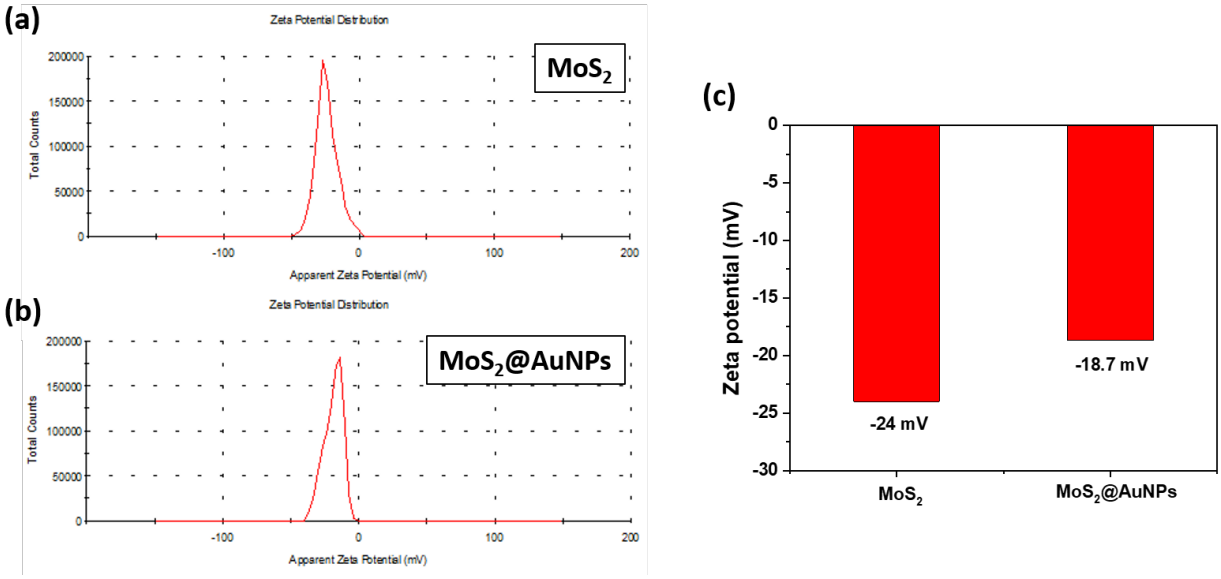

Figure 4. Zeta potential distribution of (a) MoS_2 aqueous dispersion and (b) Au-MoS_2 aqueous dispersion; (c) zeta potentials of MoS_2 dispersion before and after functionalization with Au NPs.

3.3 Structural characterizations of MoS_2 and Au-MoS_2

3.3.1 Structural study by XRD data analysis

The structural characterizations of the as-exfoliated MoS_2 NSs and Au decorated-MoS_2 NSs were performed with XRD and Raman spectroscopy. Figure 5 presents typical XRD patterns of the exfoliated MoS_2 NSs, Au-MoS_2 NSs and Au NPs. Both MoS_2 NSs and Au-MoS_2 NSs possess broad diffraction peaks corresponding to the hexagonal structure (2H) of MoS_2 (**JCPDS:37-1492**). From the Bragg's diffraction law $2d \sin\theta = n\lambda$, it can be concluded that the main peaks at 14.4°, 44.1° and 60.1° are ascribed to lattice planes (002), (006), (008) of 2H structure of MoS_2 (**JCPDS:37-1492**), which remained unchanged both in position and in shape, indicating that the decoration with Au NPs does not cause any distortion to the crystal structure of MoS_2 NSs. The peaks that appear at 38.2° and 44.4° correspond to the planes (111) and (200) of Au NPs (**JCPDS: 04-0784**), suggesting that the formed Au NPs are well crystallized.[26] The average size of Au NPs can be calculated by applying Debye-Scherrer's equation using the peak at 38° of the plane (111), and the average size was found to be 7.3 nm. The absence of impurity peaks in the X-ray diffractograms of the pristine MoS_2 NSs and Au-MoS_2 NSs should be highlighted, demonstrating the sample purity.

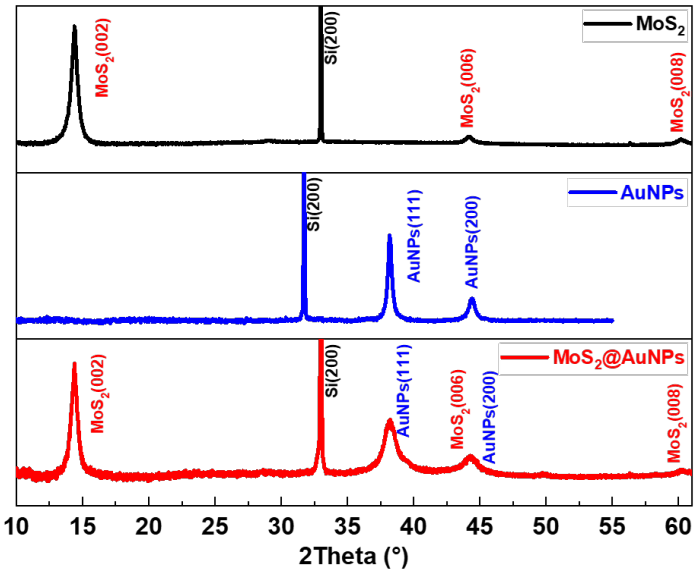

Figure 5. XRD spectra of pristine MoS_2 NSs, Au NPs, and Au-MoS_2 films prepared by being drop-casted on Si wafer (100).

3.3.2 Raman spectroscopy study

The Raman spectra of pristine MoS_2 NSs and Au NPs-decorated MoS_2 NSs, recorded at the excitation wavelength of 532 nm, are shown in Figure 6. These Raman spectra reveal characteristic peaks of MoS_2 at 383.8 $cm^{-1}$and 408.8 cm^{-1}, which agree well with the previously reported data [21]. The two vibration peaks E^1_{2g} and A_{1g} at 383.8 cm^{-1} and 408.8 cm^{-1} present in the pristine sample represent the in-plane vibration of Mo and S atoms, and the out-of-plane vibrations of S atoms respectively. Upon the functionalization with Au NPs, the two characteristic peaks are redshifted by around 1.2 to 5.5 cm^{-1} depending on the analyzed area, as shown in Figure 6 (b). This is an indicator suggesting a n-type doping by an electron transfer from Au NPs towards MoS_2 NSs, which increases the electron concentration. These observations agree with previous studies demonstrating that decoration of MoS_2 with Au NPs causes n-type doping. [18, 27]

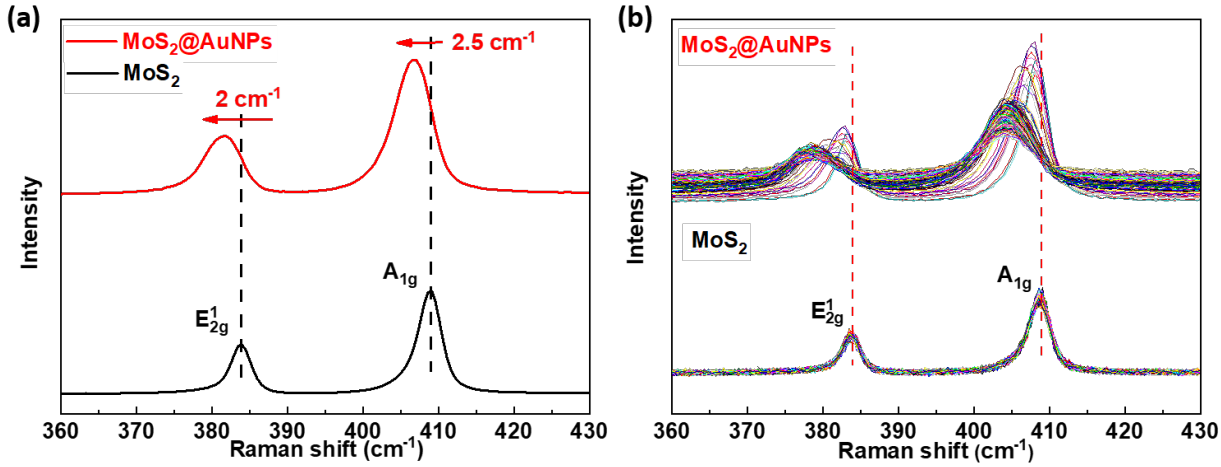

Figure 6. (a) Raman spectrum of MoS_2 NSs and Au-decorated MoS_2 NSs; (b) Raman mapping spectra of a selected area of 5 µm x 5 µm of MoS_2 thin film and Au-decorated MoS_2 thin film surface.

3.3.3 X-ray photoelectron spectroscopy study

XPS was performed to investigate the element compositions and chemical states of MoS_2 thin films before and after decoration with Au NPs as well as the electronic interaction at the Au-MoS_2 interface. As can be observed in Figure 7 (a), the surface chemical analysis confirms the presence of Mo and S in both MoS_2 and Au-MoS_2 samples, and in the spectrum of Au-MoS_2, there is also the Au peaks besides the peaks of Mo and S, which confirms the formation of Au NPs on MoS_2 NSs. Moreover, the

binding energy of O element is located at 533.2 eV, which is due to the adsorption of oxygen-containing materials such as H_2O, CO_2 and O_2 on the sample surface. [28,29] Figure 7 (b) exhibits the high-resolution spectrum of Au 4f of Au-MoS_2 sample, which after deconvolution shows two distinct peaks at 87.6 eV and 83.9 eV, referring to Au $4f_{5/2}$ and Au $4f_{7/2}$, respectively, which correspond to elemental Au , proving that Au NPs are not oxidized [18,30].

Then we compared the peak shifts of Mo and S before and after functionalization, as shown in Figure 7 (c) and (d). In MoS_2 sample, S 2p peaks are located at 163.2 eV (S $2p_{1/2}$) and 162 eV (S $2p_{3/2}$), and Mo (IV) 3d peaks of MoS_2 are observed at 232.4 eV (Mo $3d_{3/2}$) and 229.2 eV (Mo $3d_{5/2}$) with two minor peaks of Mo (VI) at 235.6 eV and 232.5 eV, corresponding to the slight oxidation of MoS_2 to MoO_3 on the surface [31]. After functionalization with Au NPs, all peaks of S and Mo slightly shifted to a higher energy level, which is directly attributed to the n-type doping process of Au NPs [32], confirming the Raman spectroscopy observations. In addition, in S 2p spectrum, we can discern two minor peaks at a lower binding energy level and they are attributed to S-Au bonds [33].

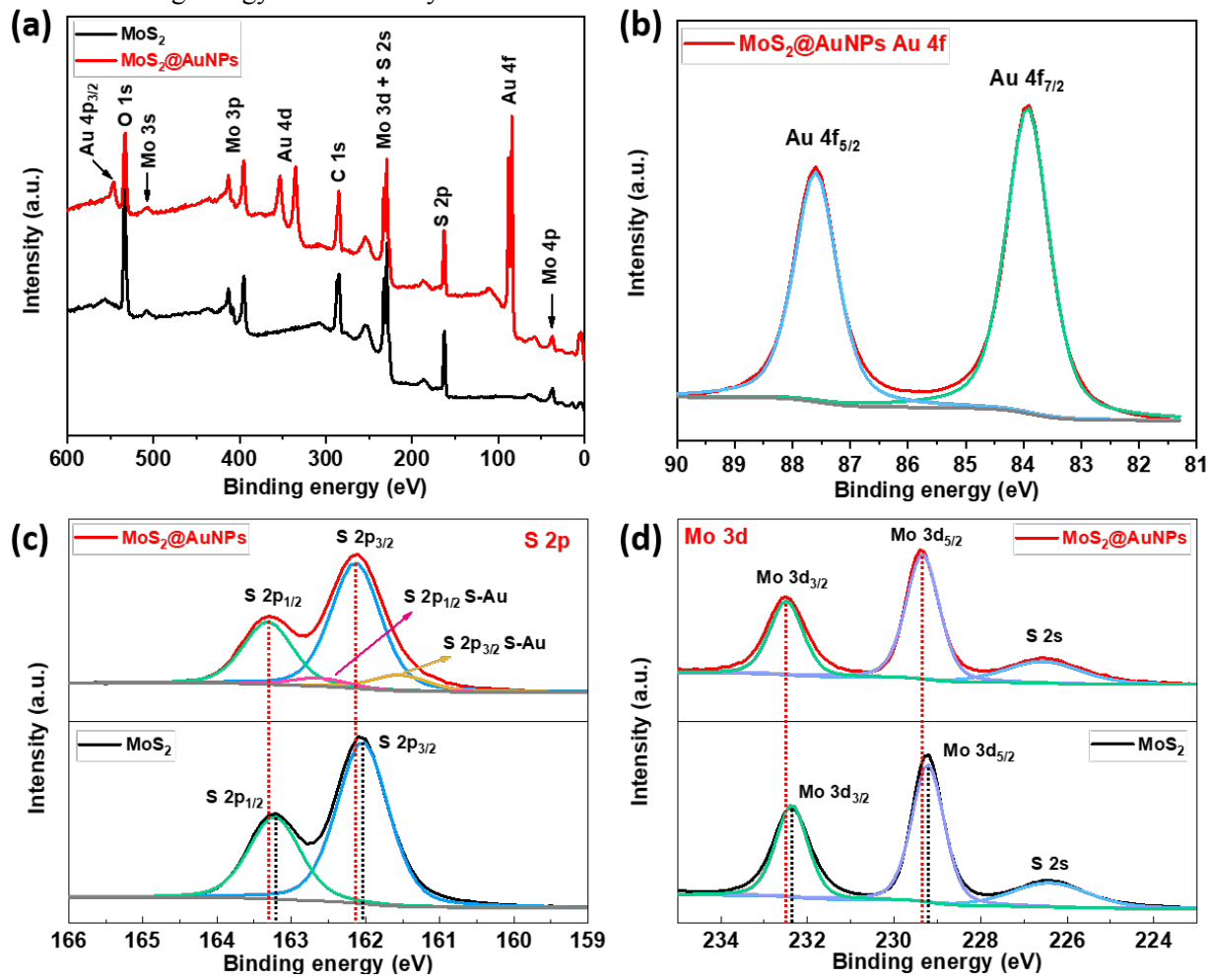

Figure 7. (a) XPS spectra of MoS_2 and Au-MoS_2; XPS spectra of (b) Au 4f for Au-MoS_2; XPS comparison of (c) S 2p and (d) Mo 3d for MoS_2 and Au-MoS_2.

3.4 Morphology and microstructure study

3.4.1 High resolution transmission electron microscopy

To investigate the crystallinity and size of Au NPs decorated MoS_2 NSs, we carried out high-resolution TEM (HRTEM). The TEM image in Figure 8 (a) shows the presence of Au NPs on the surface of MoS_2 NSs. The HR-TEM image of the Au NPs-decorated MoS_2 NSs, shown in Figure 8 (b), clearly reveals that most of the decorating Au NPs have a spherical shape, and there are mainly two populations of Au NPs with two different average NPs sizes. One population with a smaller mean size, NPs with a diameter in the range of 1-4 nm. However, for the second population, the histogram in Figure 8 (c) shows a broader dispersion in the NP size. The NPs are in the range of 5–30 nm with average diameter

size of 15 nm. The formation of large NPs has been attributed to clustering of small Au NPs or Ostwald ripening.[33] Furthermore, as observed in Figure 8 (d) a high Au NPs density with a small particle size is observed on the edge of the MoS_2 NSs, this could be related to a high content of electrons-rich defects on the edges of MoS_2 NSs, which serve as nucleation sites for the growth of small Au-NPs. [33]

To gain more insights into the structural parameters, we verified the gold lattice spacing by analyzing the HR-TEM image (Figure 8 (e) and (f)). The Au NPs decorated MoS_2 NSs showed fringe with d-spacings of 0.207 nm and 0.236 nm (Figure 8 (f)), as calculated by fast Fourier transform (FFT). This distance corresponds to the spacing between (200) plane of face centered cubic (fcc) gold (**JCPDS: 04-0784**).

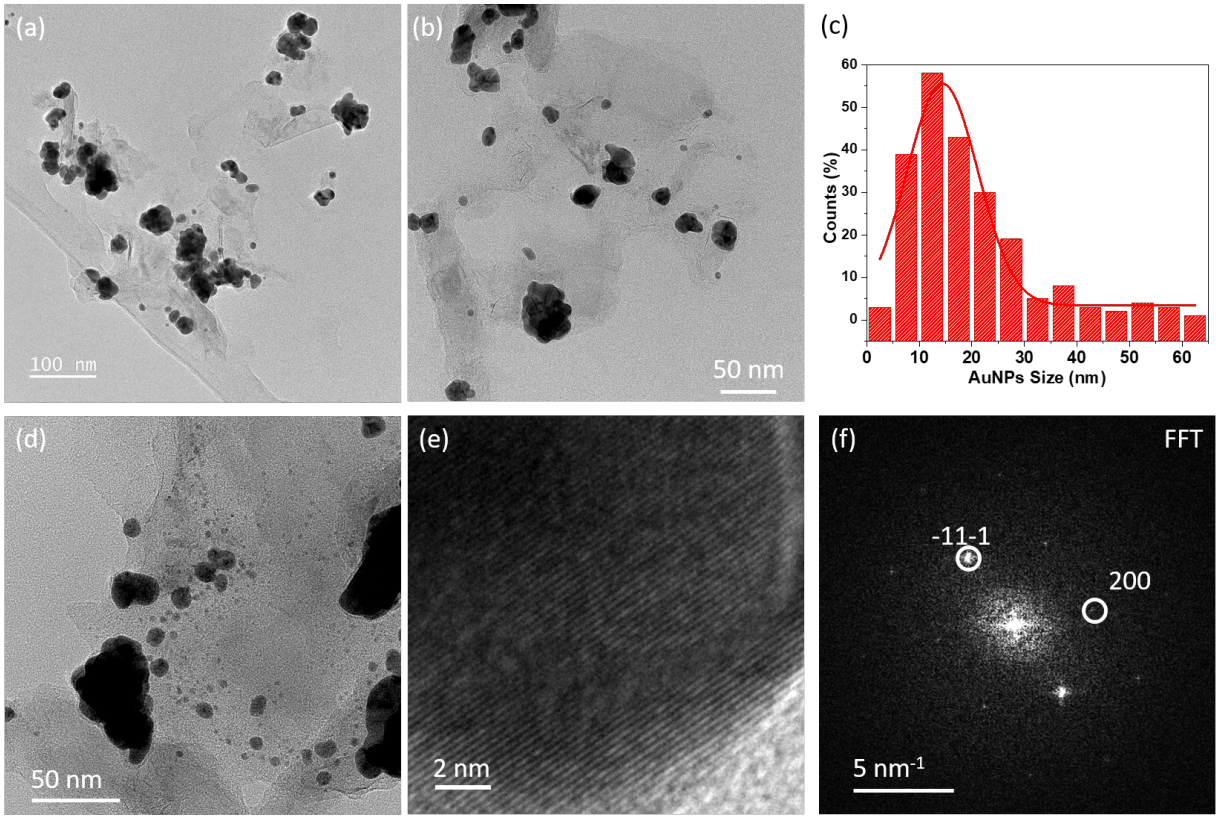

Figure 8. (a) (b) and (d) TEM images of Au-decorated MoS_2 NSs; (c) statistical plot of size distribution of Au NPs deposited on MoS_2 NSs; (e) HR-TEM image of Au lattice fringes; (f) fast Fourier transform pattern of Au (200) plane.

3.4.2 Scanning electron microscopy analysis

The surface morphology of the Au NPs-decorated MoS_2 NSs thin film was analyzed using SEM and AFM. SEM images of MoS_2 NSs thin film and Au NPs-decorated MoS_2 NSs thin film are presented in Figure 9. MoS_2 thin film surface functionalization with Au NPs was carried out by dip-coating method described in detail in Material and Method Section 2.2. From the image of pristine MoS_2 NSs thin film, one can observe that the MoS_2 NSs film is uniformly deposited without the formation of any noticeable cracks, even at a large scale, the sizes of MoS_2 NSs are around 100-150 nm. Once functionalized with Au NPs using dip-coating method, the presence of Au NPs on MoS_2 NSs can be easily observed. The shape and size of MoS_2 NSs remain unchanged which indicates that the functionalization with Au NPs doesn't change the morphology of MoS_2 NSs.

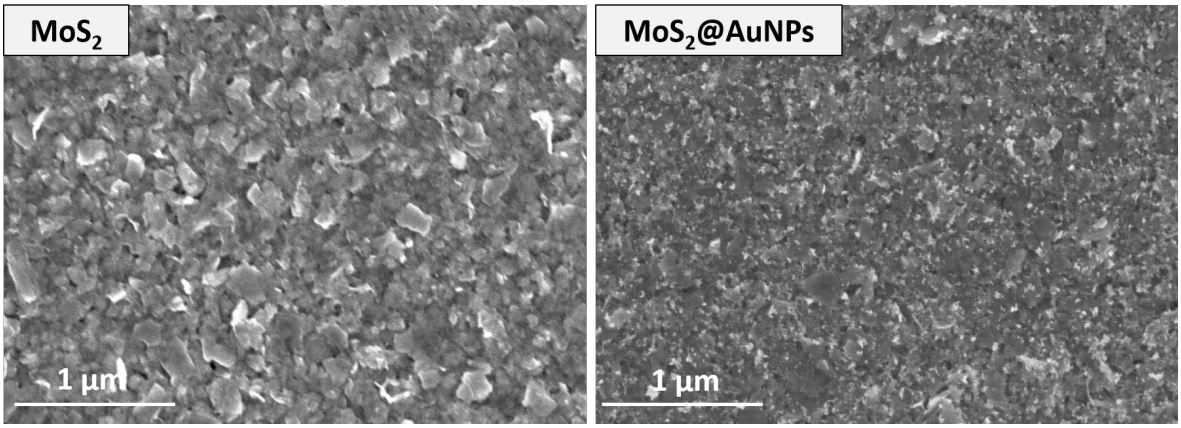

Figure 9. SEM images of pristineMoS_2 NSs thin film and Au NPs-decorated MoS_2 NSs thin film.

3.4.3 Atomic force microscopy analysis

Figure 10 shows the AFM image of Au NPs-decorated MoS_2 NSs thin film obtained using ScanAsyst mode. On the right hand side of the image, there are two magnified images of MoS_2 NSs, on top of which deposited Au NPs. These two images also demonstrate the high density of Au NPs on MoS_2 NSs, mostly oval. The size of the Au NPs can be calculated by NanoScope Analysis where the horizontal size ranges from 10 nm to 20 nm and the vertical size ranges from 5 nm to 10 nm respectively, which are in the range of the Au NPs size obtained from TEM.

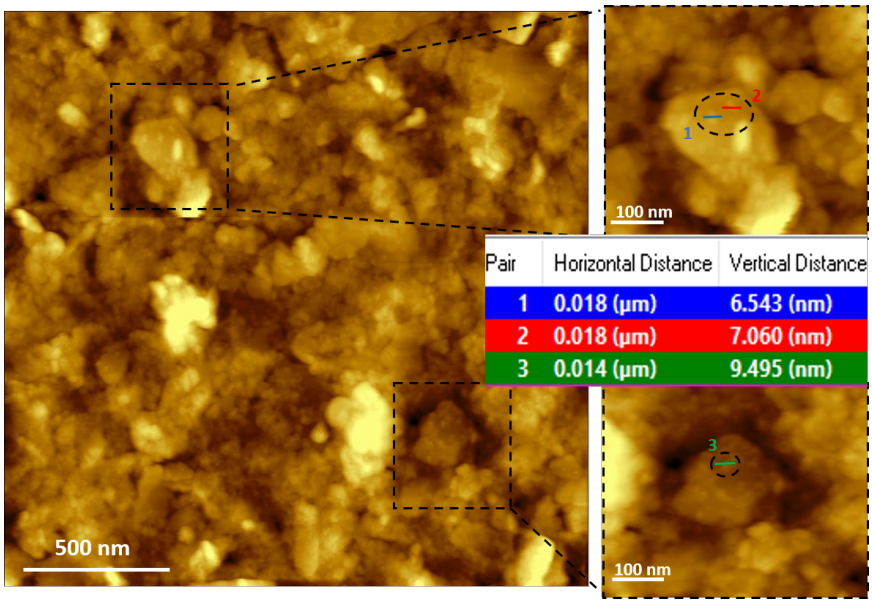

Figure 10. AFM image of Au NPs-decorated MoS_2 thin film.

3.5 NO_2 sensing performance

To understand the gas sensing capabilities of pristine MoS_2 and Au-functionalized MoS_2 films, it is essential to first analyze their electrical characteristics. This is achieved by performing current-voltage (I-V) measurements at room temperature (RT), using two-point probe, with an applied bias voltage between −10 V and +10 V. As shown in Figure 11 (a), both films exhibited an excellent Ohmic behavior, confirming their excellent electrical properties. Au NPs-decorated MoS_2 film manifested a lower resistance with the current in the range of nano-amperes as does the unfunctionalized MoS_2 thin film, one can argue that the primary pathway for charge transport is through MoS_2 NSs thin film. According to the slope of the I-V curves, the resistance of Au NPs-decorated MoS_2 film is 0.86 GΩ which is smaller than the resistance of pure MoS_2 (1 GΩ). The resistance decrease observed is believed owing to the doping effect which induces change in Fermi level and charge transfer between Au NPs

and MoS_2 NSs. These results are in agreement with the observations obtained from Raman and XPS experiments, which confirm that the Au NPs causes n-type doping on MoS_2.

Then we investigated the NO_2 sensing performances of pure and Au-decorated MoS_2 thin films towards low concentrations of NO_2 gas (1 ppm to 3 ppm). The measurements were conducted by recording the resistance change over time at an applied voltage of 10 V and a temperature of 30 °C. Figure 11 (b) and (c) show the resistance variation of the sensors as a function of time with increasing concentrations of NO_2 gas at 30 °C. Overall it is evident that the MoS_2 films exhibit stable and reproducible responses versus NO_2 gas molecules. Upon exposure to NO_2 gas, the resistance of pristine MoS_2 films decreased. This is consistent with NO_2 being an electron acceptor and when NO_2 molecules are adsorbed onto the MoS_2 NS surface, they extracted electrons from the conduction band of MoS_2, which increases the hole carrier concentration. This behavior leads to a decrease in the resistance, indicating p-type semiconducting behavior. Similar to pristine MoS_2, the Au-decorated MoS_2 films also exhibited a decrease in resistance upon exposure to NO_2. This suggests that the Au decoration does not alter the fundamental p-type semiconducting nature of the LPE MoS_2 films. These outcomes confirm the p-type semiconducting behavior of LPE MoS_2 NSs and grafting of Au NPs on the MoS_2 NSs does not change the type of charge carriers. Moreover, from dynamic sensing curves in Figure 11 (b) and (c), it is possible to obtain information regarding the response and recovery behaviors of the MoS_2 and Au-MoS_2 thin film sensor. MoS_2 sensors showed a good and fast response to NO_2 gas (2.2% to 1 ppm NO_2 within 76 s as shown in Figure 11 (d)). However, during sensing measurements, and repeated operation, a significant drift in baseline is observed in MoS_2 sensor, as seen in Figure S1. The drift in baseline resistance is due to the desorption which does not fully occur resulting a partial recovery of sensing layer. After decoration with Au NPs, the Au-MoS_2 sensor displayed an improved performance with increased response to NO_2 gas and complete recovery (5.6% response to 1 ppm NO_2, response/recovery time ~ 121 s / 32 mins in Table 1). Mostly important, as resumed in Figure 11 (d) and Table 1, the slow rates of response and recovery at RT of pristine MoS_2 suggest defect-dominated adsorption, the Au-decorated sensor shows a full recovery within 1 hour and the response to NO_2 gas increased at least 2 times than the pristine MoS_2 sensor, which should be considered as a better sensing materials. Furthermore, we tested the ability of MoS_2 and Au-MoS_2 sensor to detect 0.5 ppm NO_2 (Figure S2), the results demonstrate the high sensitivity of the fabricated sensors to low gas concentrations. To investigate the potential effect of NO_2 on the structure of Au-MoS_2 sensor, we performed and compared the SEM and XRD analyses of Au-MoS_2 thin films before and after the exposure to NO_2. From the according results shown in Figure S3, we can see that there is no structure change of Au-MoS_2 sensor.

To assess sensing performance of our devices, we list in table S1 in SI the gas sensing response/recovery time results for a variety of 2D materials reported by other research groups. One can see that our Au-MoS_2 based NO_2 gas sensors do have reasonable response/recovery times and are quite promising. Furthermore, the fully recover to the baseline did not require any auxiliary conditions, ultraviolet or heating treatment.

Figure S4 in SI shows the dynamic response curves of as-fabricated Au-MoS_2 gas sensors measured under 1ppm, 2 ppm and 3 ppm NO_2 at room temperature. As evidenced from the Figure S4, the device exhibits a good response reproducibility under NO_2 with various concentrations during repeated cycles. Moreover, the long-term stability of Au-MoS_2 based sensor has been tested, the results revealed that Au-MoS_2 sensor had a relatively good long-term stability and its response remained at 80% of the response of fresh sensor toward 3 ppm of NO_2 after 180 days of storage, as displayed in Figure S5 in SI.

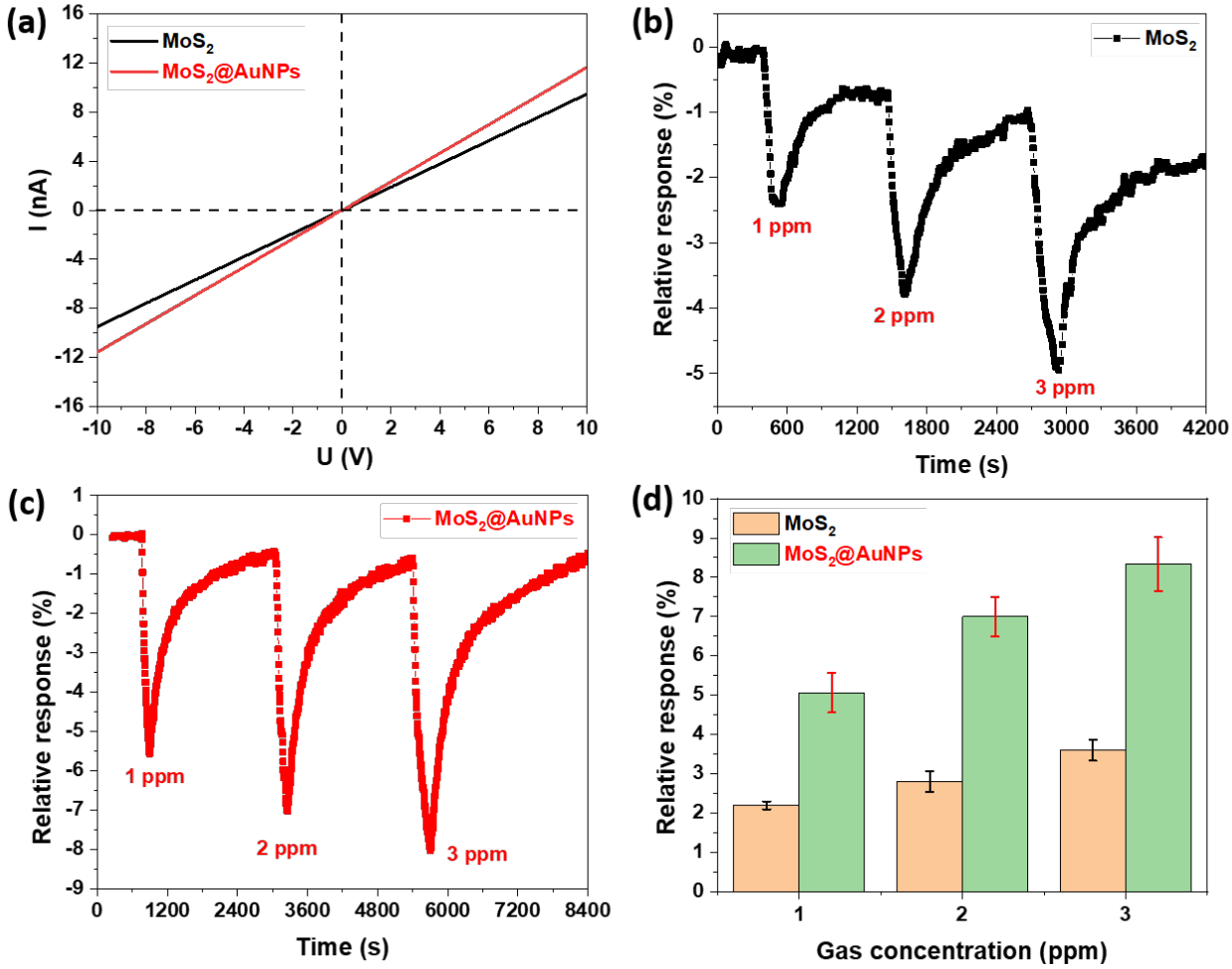

Figure 11. (a) I-V curves of MoS_2 and Au-MoS_2 thin films; (b)(c) Sensing transient of MoS_2 and Au-MoS_2 thin film sensors to different NO_2 concentration; (d) Response comparison of MoS_2 and Au-MoS_2 thin film sensors.

Table 1. Resume of response/recovery times of MoS_2 and Au-MoS_2 sensor to NO_2 gas

[NO_2]	**1 ppm**	**2 ppm**	**3 ppm**
MoS_2	76 s/ -	126 s/ -	220 s/ -
Au-MoS_2	121 s/ 32 mins	180 s/ 32 mins	270 s/ 40 mins

To better understand the reversibility of sensors, we quantitatively analyzed reaction kinetics of MoS_2 sensor and Au-MoS_2 sensor. We calculated the adsorption rate constant (k_{ads}), the desorption rate constant (k_{des}) and the equilibrium constant ($K = k_{ads}/k_{des}$) by fitting sensitivity curves in Figure 12 (a) to (f) to Equation (2) and (3) using adsorption and desorption kinetic models [34]:

$$S(t) = S_0 \exp(-k_{des} t) \qquad (1)$$

$$S(t) = S_{max} \frac{C_a K}{1 + C_a K} \left[1 - \exp\left(-\frac{1 + C_a K}{K} k_{ads} t\right)\right] \qquad (2)$$

where S_0 represents the sensitivity after the removal of NO_2, S_{max} is the maximum sensitivity to NO_2, and C_a is the concentration of NO_2. The calculated adsorption rate, desorption rate, and equilibrium constants of MoS_2 sensors before and after functionalization of Au NPs at different NO_2 concentrations are summarized in Table 2. The adsorption rate constants and desorption rate constants of MoS_2 sensor before and after functionalization remain in the same order of magnitude. The desorption rate constants in the first and second reaction states were fitted independently to precisely quantify the rate constants

and minimize the variance from the measured data [35]. The decoration of Au NPs seems not to significantly affect the adsorption and first desorption of NO_2. In the second desorption process, we can observe that the desorption rate constants of Au-MoS_2 sensor are overall higher than those of pure MoS_2 sensor. Especially for 3 ppm NO_2, 1.9-fold increase was achieved in desorption rate constant for Au-MoS_2 sensor, which implies reversible recovery property of Au-MoS_2 sensor. In addition, as displayed in Table 3, we compared the adsorption/desorption kinetics of our MoS_2 and Au-MoS_2 sensors with other sensing materials previously reported in literature, demonstrating rapid response/recovery characteristics of the sensors fabricated through this work.

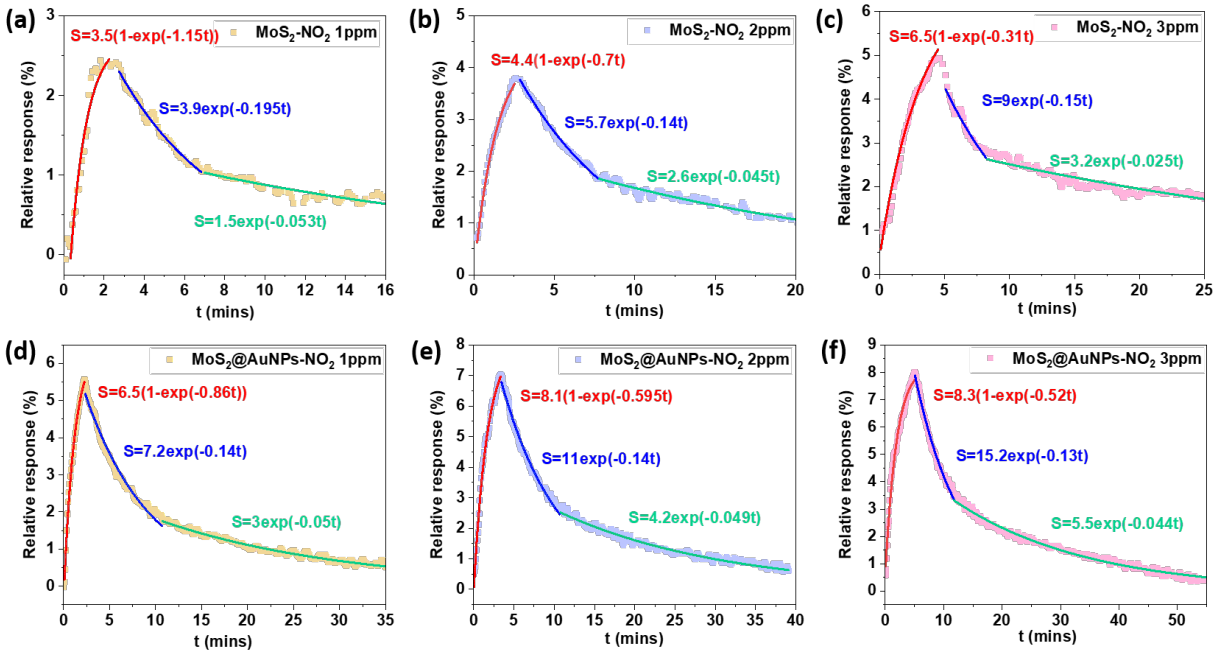

Figure 12. Dynamic response and recovery curves of (a–c) MoS_2 sensor and (d–f) Au-MoS_2 sensor based on adsorption and desorption kinetics at different NO_2 concentration.

Table 2. Adsorption rate constant (k_{ads}), desorption rate constant (k_{des}) and equilibrium constant ($K = k_{ads}/k_{des}$) of MoS_2 sensor and Au-MoS_2 sensor to NO_2 gas.

Sensor	C_a (ppm)	k_{ads} ($ppm^{-1}\ s^{-1}$)	k_{des1} (s^{-1})	K_1 (ppm^{-1})	k_{des2} (s^{-1})	K_2 (ppm^{-1})
MoS_2	1	1.91×10^{-2}	3.25×10^{-3}	5.9	7.17×10^{-4}	21.7
	2	5.83×10^{-3}	2.33×10^{-3}	2.5	7.17×10^{-4}	8.14
	3	2.5×10^{-3}	2.5×10^{-3}	1	3.83×10^{-4}	6.52
MoS_2@AuNPs	1	1.43×10^{-2}	2.33×10^{-3}	6.14	8.33×10^{-4}	17.2
	2	5×10^{-3}	2.33×10^{-3}	2.14	8.33×10^{-4}	6
	3	2.83×10^{-3}	2.17×10^{-3}	1.31	7.33×10^{-4}	3.86

Table 3. Comparison of NO_2 sensing kinetic constants of sensors based on different materials previously reported in literature.

Sensor	Synthesis method	T (°C)	Target	C_a (ppm)	k_{ads} ($ppm^{-1}\ s^{-1}$)	k_{des1} (s^{-1})	K_1 (ppm^{-1})	k_{des2} (s^{-1})	K_2 (ppm^{-1})	Ref.
p-MoS_2	Liquid exfoliation	30	NO_2	2	5.83×10^{-3}	2.33×10^{-3}	2.5	7.17×10^{-4}	8.14	This work
MoS_2@AuNPs					5×10^{-3}	2.33×10^{-3}	2.14	8.33×10^{-4}	6	
n-MoS_2	Hydrothermal synthesis	r.t	NO_2	10	1.5×10^{-4}	5.21×10^{-5}	2.88			[36]
N doped MoS_2					1.77×10^{-2}	2.68×10^{-2}	0.66			
Ag NWs	Polyol method	r.t	NO_2	20	4.65×10^{-2}	4.56×10^{-3}	10.2			[37]

r-GO	Hummer's method	100	NO_2	20	8.85×10^{-3}	1.34×10^{-3}	6.07	1.15×10^{-3}	46.59	[38]
SWNT/PdO-Co_3O_4		22	NO_2	20	2.12×10^{-3}	1.72×10^{-3}	1.23			[39]
SWNT	Thermal decomposition of $Fe(CO)_5$	30	DMMP	1.5	3.66×10^{-2}	0.525	0.0698			[40]

Investigating the effect of interfering gases on the sensor response, particularly volatile organic compounds (VOCs), can help to establish a better understanding of its potential for future implementation in real-word of gas monitoring. As a consequence, the responses of MoS_2 sensor and Au-MoS_2 sensor to volatile organic compounds (VOCs), such as benzene, hexane and toluene, have been studied (the dynamic responses to the VOCs are shown in Figure S6). From the response histogram displayed in Figure 13, it is clear that both MoS_2 sensor and Au-MoS_2 sensor have nearly no response towards benzene, MoS_2 sensor is approximately as sensitive to hexane and toluene as to NO_2, while the sensitivity to these two gases is reduced after functionalization with Au NPs. All these results demonstrate that the functionalization with Au NPs holds a great promise to enhance the selectivity of MoS_2 sensor to NO_2 gas.

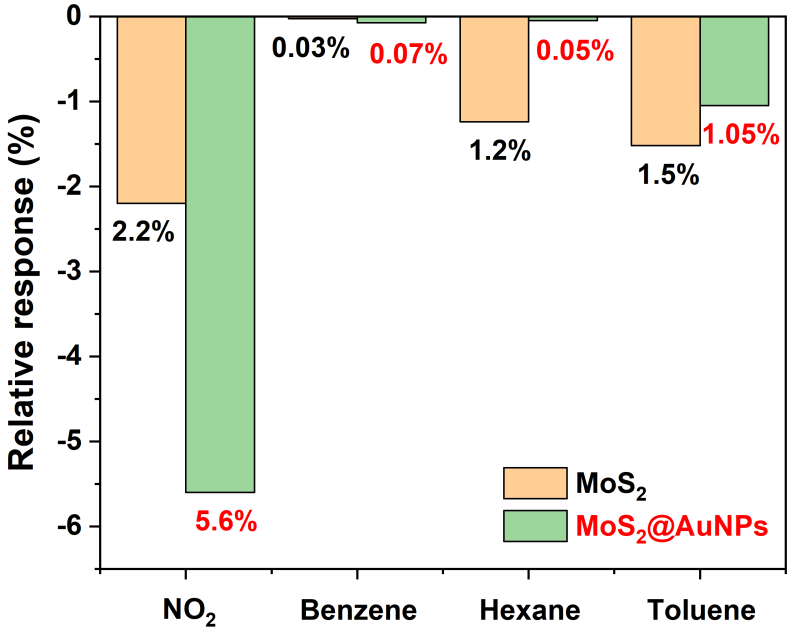

Figure 13. Histogram of selectivity comparison of MoS_2 and Au-MoS_2 gas sensors toward different VOC gases.

To evaluate the effect of humidity on the NO_2 sensing properties of Au-MoS_2 based gas sensors, the sensor was exposed to 0.5 ppm of NO_2 at various relative humidity (RH%) levels ranging from 10% to 90%. The humidity was adjusted in 20% increments with a ramping rate of 30% min^{-1} at RT, as shown in Figure 14. Initially, the baseline resistance increases sharply as RH% arises from 10% to 30% RH (Figure S7). Numerous researches have been dedicated in investigation of humidity sensor based on MoS_2, the sensing performance is controversial in terms of conductivity increase or decrease as a function of RH%. In our case, the baseline resistance initially increases sharply as RH% arises from 10% to 30% RH (Figure S7), similar to previous reports [41, 42]. Between 30% and 70% RH, the baseline resistance stabilizes. The sensor's response to NO_2 remains relatively stable at 2.1% across this RH range. However, at higher humidity levels, the sensor response decreases. This reduction can be explained by the formation of a water film on top of the sensing layer, which limits the interaction between the gas and the sensing material. Similar results were previously reported by Sun et al. [43].

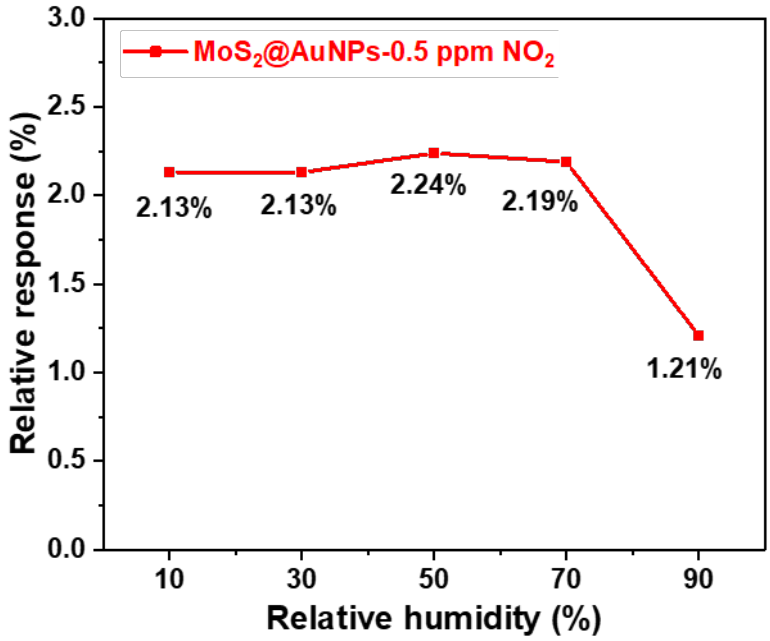

Figure 14. The effect of relative humidity on the sensing performance of Au-MoS_2 sensor.

3.6 Gas sensing mechanism

The NO_2 sensing mechanism can be qualitatively analyzed by using space charge model. According to this model, adsorbed oxygen has a crucial effect on the sensing mechanism. Regarding pure MoS_2 sensor, and according to this model, firstly when MoS_2 NSs are exposed to air, the oxygen molecules are adsorbed on the MoS_2 surface, particularly at defect sites such as sulfur vacancies, taking electrons from MoS_2. This electron transfer process leads to the formation of oxygen ions (O_2^-) on the surface. It should be noted that the nature of the adsorbed oxygen species depends on temperature, O_2^- (<150 °C), O^- (150−400 °C), and O^{2-} (>400 °C). Having that in mind the gas sensing measurements were performed at RT, therefore the O_2^- is the predominant adsorbed species. The as-adsorbed oxygen molecules cause the extraction of electrons from the valence band of MoS_2, resulting in the formation of a hole accumulation layer (HAL) in the valence band, as depicted in Figure S8 (b). This reaction can be represented by the following equations:

$$O_{2(gas)} \rightarrow O^-_{2(ads)} + h^+ \quad (3)$$

$$NO_{2(gas)} \rightarrow NO^-_{2(ads)} + h^+ \quad (4)$$

$$NO_{2(gas)} + O^-_2 \rightarrow NO^-_{3(ads)} + O^- + h^+ \quad (5)$$

Then when the sensor is exposed to NO_2 molecules, the spontaneously adsorbed NO_2 electrophilic molecules extract electrons from MoS_2 valence band, and form NO_2^- and holes, as well as the reaction of NO_2 molecules with the chemisorbed oxygen species present at the surface, also increases the concentration of holes in the HAL (Figure S8 (c)). As a consequence, the resistance of the MoS_2 layer decreases.

In the case of MoS_2 functionalized with Au NPs, heterojunction formation between MoS_2 and Au NPs is a key parameter for enhancing the sensing properties through the modulation of HAL. As depicted in Figure 15, at the interface of MoS_2 NSs and Au NPs heterojunction, the electrons are transferred from Au NPs to MoS_2 till the alignment of the Fermi levels of MoS_2 and Au at equilibrium state [44] since the work function of MoS_2 is higher than that of Au (5.4 eV for MoS_2, 5.1 eV for Au), which makes Au NPs as an excellent n-type dopant. This would lead to the formation of a HAL in the valence band. Similarly, the NO_2 sensing mechanism of Au-MoS_2 sensor is the same as that of the bare MoS_2 sensor. As does for the case of bare MoS_2 sensor, oxygen molecules in air adsorb onto the surface of MoS_2 and capture electrons from it, then forming chemisorbed O_2^- species. After the electrons

extraction process, the hole carrier concentration increases in the HAL, which results a decrease in the resistance of the Au-MoS_2 sensor. When introducing NO_2 molecules, the NO_2 capture more electrons to form the NO_2^-, which results more electrons extraction and enlargement of HAL. Also as NO_2 has higher electron affinity than O_2 and their subsequent redox reaction results in electron capturing process (equation 5), thus increasing hole concentration on Au-MoS_2's surface, thereby causing a reduction of the MoS_2-Au sensor's resistance. Moreover, the catalytic effect of Au NPs can further improve the sensing performance of Au-MoS_2 sensor. The Au NPs can promote the dissociation of O_2 adsorbed on MoS_2 surface, offering more active sites accessible for the adsorption of NO_2 [16] or absorb more NO_2 molecules on MoS_2 surface through charge transfer [45], thus enhancing the response to NO_2.

Regarding the enhancement of recovery property of Au-MoS_2 sensors, it has been proven that the adsorption of gas molecules can be categorized into two types: physisorption of NO_2 that occurs at low energy binding sites of defect-free MoS_2 sensing layer, and chemisorption of NO_2 which takes place on the defect sites of MoS_2 NSs [46]. For pure MoS_2 sensor, the NO_2 molecules have tendency to adsorb in the defects at the edge which possess strong binding energy to NO_2 gas molecules [47], making them difficult to evacuate during the recovery process, so that a baseline drift of response to NO_2 occurs for pure MoS_2. After the functionalization with Au NPs, we can observe from TEM images that the growth of the NPs on the surface of the MoS_2 NSs took place at the defect sites, mainly located at the edges of the NSs, converting edge defects to catalytically-active disulfide [33] and reducing the number of defect sites available for the chemisorption process, which promotes the full recovery of NO_2 response process.

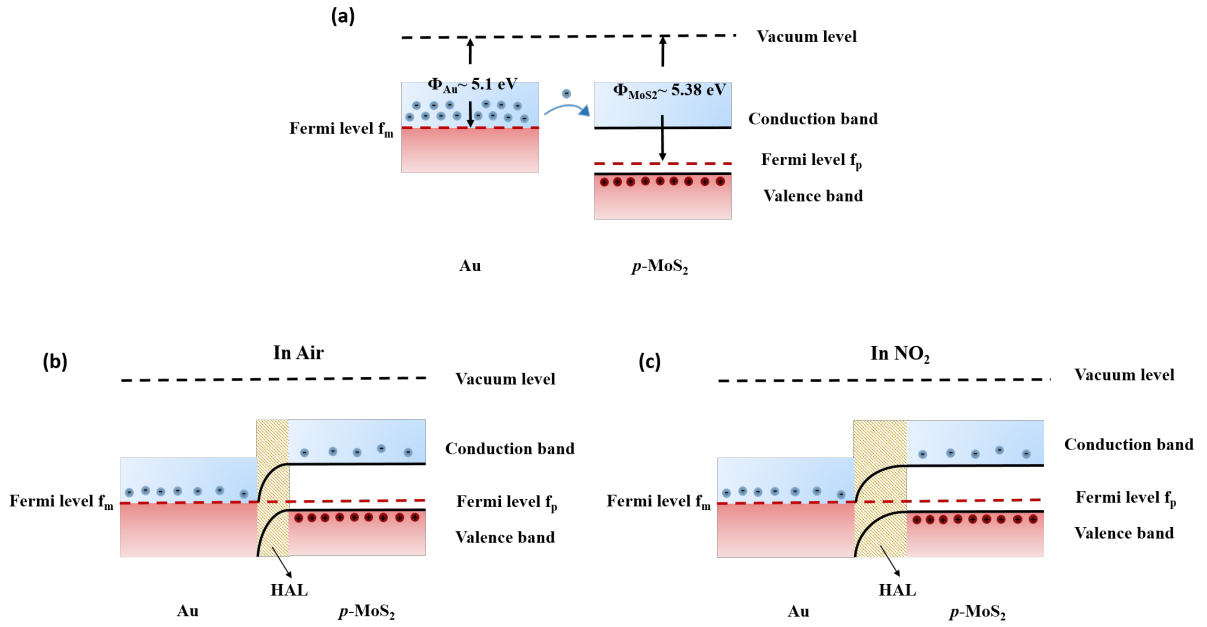

Figure 15. Schematic illustration of Au NPs n-type doping on MoS_2 (a) before contact, (b) after contact in air and (c) after contact in NO_2.

4. Conclusion

In summary, we have reported the functionalization of MoS_2 NSs with Au NPs. MoS_2 NSs were fabricated by liquid shear exfoliation. A spontaneous reaction between $HAuCl_4$ and MoS_2 NSs without any reducing agents results in the formation of Au NPs preferentially at edges and terraces of exfoliated MoS_2, with two populations of different sizes: one of 1 nm to 4 nm, and the other one of 5 nm to 30 nm. By decorating with Au NPs, MoS_2 sensor showed a significantly enhanced sensitivity toward NO_2 gas, and an improvement in the recovery rate. The decoration of Au NP on MoS_2 NSs is primarily responsible for the improved sensor performance, because it not only enhances the electrical characteristics of MoS_2 but also provides a spillover catalytic effect for NO_2 sensing. However, the decoration of Au NPs doesn't affect the adsorption and desorption rate of NO_2. From the microscopic images, it is clear that the growth of Au NPs mainly takes place on the defects of MoS_2 surface, leading to the reduction of chemisorption sites of NO_2 on MoS_2 NSs, which aids to a fast fully recovery to the baseline. We highly believe that the functionalization of the TMDs NSs with metal NPs, via liquid phase method to improve the

sensitivity, fast response and full response-recovery for gas detection at RT, can promote the development of enhanced chemiresistive gas sensors based on 2D TMDs.

Author Contributions: Conceptualization, F.B., A.Y.; Investigation, P.N., E.M., K.D., D.D., F.B. and A.Y.; Validation, F.B., A.Y.; writing-original draft preparation, P.N., F.B., A.Y.; writing—review and editing, P.N., F.B., A.Y.; All authors have read and agreed to the published version of the manuscript."

Funding:

The authors acknowledge financial support from the French state managed by the National Research Agency(ANR-23-CE04-0004).

Institutional Review Board Statement:

"Not applicable".

Informed Consent Statement:

"Not applicable".

Data Availability Statement: Not applicable.

Acknowledgments: The electrical characterizations, part of this work benefited through the use of the PLATINE platform, from the support of the Ecole Polytechnique fund raising Smart Environments: Nanosensors and Nanoreliability Initiative. The authors acknowledge the help and support from Dr. Rabei Mohammedi for DLS measurements, Dr. Simons Hallais for AFM analysis, Dr. Sandrine Tusseau-Nenez for XRD analysis. P.N. thanks China Scholarship Council (CSC) for her Ph.D. scholarship n°202108070156.

Conflicts of Interest: The authors declare no conflict of interest.

References

(1) Tang, M. Y.; Wang, Y. Y.; Shen, H.; Che, G. B. Solution-Based Preparation Techniques for Two-Dimensional Molybdenum Sulfide Nanosheet and Application of Its Composite Materials in Photocatalysis and Electrocatalysis. *Progress in Chemistry* **2018**, *30* (11), 1646-1659. DOI: 10.7536/pc180109.
(2) Hu, C.-X.; Shin, Y.; Read, O.; Casiraghi, C. Dispersant-assisted liquid-phase exfoliation of 2D materials beyond graphene. *Nanoscale* **2021**, *13* (2), 460-484, 10.1039/D0NR05514J. DOI: 10.1039/D0NR05514J.
(3) Liao, L.; Kovalska, E.; Regner, J.; Song, Q.; Sofer, Z. Two-Dimensional Van Der Waals Thin Film and Device. *Small* **2024**, *20* (4), 2303638. DOI: https://doi.org/10.1002/smll.202303638.
(4) Jeong, Y.; Samorì, P. Functionalized 2D transition metal dichalcogenide inks via liquid-phase exfoliation for practical applications. *Bulletin of the Korean Chemical Society* **2024**, *45* (2), 110-124. DOI: https://doi.org/10.1002/bkcs.12807.
(5) Li, X.; Zhu, H. Two-dimensional MoS2: Properties, preparation, and applications. *Journal of Materiomics* **2015**, *1* (1), 33-44. DOI: https://doi.org/10.1016/j.jmat.2015.03.003.
(6) Liu, F.; Fan, Z. Defect engineering of two-dimensional materials for advanced energy conversion and storage. *Chemical Society Reviews* **2023**, *52* (5), 1723-1772, 10.1039/D2CS00931E. DOI: 10.1039/D2CS00931E.
(7) Giri, A.; Park, G.; Jeong, U. Layer-Structured Anisotropic Metal Chalcogenides: Recent Advances in Synthesis, Modulation, and Applications. *Chemical Reviews* **2023**, *123* (7), 3329-3442. DOI: 10.1021/acs.chemrev.2c00455.
(8) Kim, J.-S.; Yoo, H.-W.; Choi, H. O.; Jung, H.-T. Tunable Volatile Organic Compounds Sensor by Using Thiolated Ligand Conjugation on MoS2. *Nano Letters* **2014**, *14* (10), 5941-5947. DOI: 10.1021/nl502906a.

(9) Long, H.; Harley-Trochimczyk, A.; Pham, T.; Tang, Z.; Shi, T.; Zettl, A.; Carraro, C.; Worsley, M. A.; Maboudian, R. High Surface Area MoS2/Graphene Hybrid Aerogel for Ultrasensitive NO2 Detection. *Advanced Functional Materials* **2016**, *26* (28), 5158-5165. DOI: https://doi.org/10.1002/adfm.201601562.
(10) Kang, X.; Yip, S.; Meng, Y.; Wang, W.; Li, D.; Liu, C.; Ho, J. C. High-performance electrically transduced hazardous gas sensors based on low-dimensional nanomaterials. *Nanoscale Advances* **2021**, *3* (22), 6254-6270, 10.1039/D1NA00433F. DOI: 10.1039/D1NA00433F.
(11) Kumar, S.; Mirzaei, A.; Kumar, A.; Hoon Lee, M.; Ghahremani, Z.; Kim, T.-U.; Kim, J.-Y.; Kwoka, M.; Kumar, M.; Sub Kim, S.; Woo Kim, H. Nanoparticles anchored strategy to develop 2D MoS2 and MoSe2 based room temperature chemiresistive gas sensors. *Coordination Chemistry Reviews* **2024**, *503*, 215657. DOI: https://doi.org/10.1016/j.ccr.2024.215657.
(12) Sun, Y.; Zhang, Y. Wafer-scale floating-gate field effect transistor sensor built on carbon nanotubes film for Ppb-level NO2 detection. *Chemical Engineering Journal* **2023**, *473*, 145480. DOI: https://doi.org/10.1016/j.cej.2023.145480.
(13) Zhou, Y.; Zou, C.; Lin, X.; Guo, Y. UV light activated NO2 gas sensing based on Au nanoparticles decorated few-layer MoS2 thin film at room temperature. *Applied Physics Letters* **2018**, *113* (8). DOI: 10.1063/1.5042061 (acccessed 5/11/2024).
(14) Rahman, M. T.; Khan, R. R.; Tian, Y.; Ibrahim, H.; Dong, L. High-Sensitivity and Room-Temperature Nitrous Oxide Sensor Using Au Nanoparticles-Decorated MoS2. *IEEE Sensors Journal* **2023**, *23* (17), 18994-19001. DOI: 10.1109/JSEN.2023.3296504.
(15) Hu, J.; Liu, X.; Zhang, J.; Gu, X.; Zhang, Y. Plasmon-activated NO2 sensor based on Au@MoS2 core-shell nanoparticles with heightened sensitivity and full recoverability. *Sensors and Actuators B: Chemical* **2023**, *382*, 133505. DOI: https://doi.org/10.1016/j.snb.2023.133505.
(16) Rawat, S.; Bamola, P.; Rani, C.; Kaushik, V.; Kumar, U.; Dwivedi, C.; Rattan, R.; Sharma, M.; Kumar, R.; Sharma, H. Interdigitated electrodes-based Au-MoS2 hybrid gas sensor for sensing toxic CO and NH3 gases at room temperature. *Nanotechnology* **2023**, *34* (30), 305601. DOI: 10.1088/1361-6528/acd0b7.
(17) Kim, Y.; Sohn, I.; Shin, D.; Yoo, J.; Lee, S.; Yoon, H.; Park, J.; Chung, S.-m.; Kim, H. Recent Advances in Functionalization and Hybridization of Two-Dimensional Transition Metal Dichalcogenide for Gas Sensor. *Advanced Engineering Materials* **2024**, *26* (1), 2301063. DOI: https://doi.org/10.1002/adem.202301063.
(18) Kim, T.; Lee, T. H.; Park, S. Y.; Eom, T. H.; Cho, I.; Kim, Y.; Kim, C.; Lee, S. A.; Choi, M.-J.; Suh, J. M.; et al. Drastic Gas Sensing Selectivity in 2-Dimensional MoS2 Nanoflakes by Noble Metal Decoration. *ACS Nano* **2023**, *17* (5), 4404-4413. DOI: 10.1021/acsnano.2c09733.
(19) Sun, Y.; Wang, Y.; Chen, J. Y. C.; Fujisawa, K.; Holder, C. F.; Miller, J. T.; Crespi, V. H.; Terrones, M.; Schaak, R. E. Interface-mediated noble metal deposition on transition metal dichalcogenide nanostructures. *Nature Chemistry* **2020**, *12* (3), 284-293. DOI: 10.1038/s41557-020-0418-3.
(20) Dunklin, J. R.; Lafargue, P.; Higgins, T. M.; Forcherio, G. T.; Benamara, M.; McEvoy, N.; Keith Roper, D.; Coleman, J. N.; Vaynzof, Y.; Backes, C. Monolayer-enriched production of Au-decorated WS2 Nanosheets via Defect Engineering. *MRS Advances* **2018**, *3* (41), 2435-2440. DOI: 10.1557/adv.2018.350.
(21) Ni, P.; Dieng, M.; Vanel, J.-C.; Florea, I.; Bouanis, F. Z.; Yassar, A. Liquid Shear Exfoliation of MoS2: Preparation, Characterization, and NO2-Sensing Properties. *Nanomaterials* **2023**, *13* (18). DOI: 10.3390/nano13182502.

(22) Qiao, Y.; Chen, H.; Lin, Y.; Huang, J. Controllable Synthesis of Water-Soluble Gold Nanoparticles and Their Applications in Electrocatalysis and Surface-Enhanced Raman Scattering. *Langmuir* **2011**, *27* (17), 11090-11097. DOI: 10.1021/la2019154.
(23) Choi, S.; Shaolin, Z.; Yang, W. Layer-number-dependent work function of MoS2 nanoflakes. *Journal of the Korean Physical Society* **2014**, *64* (10), 1550-1555. DOI: 10.3938/jkps.64.1550.
(24) Kim, J.; Byun, S.; Smith, A. J.; Yu, J.; Huang, J. Enhanced Electrocatalytic Properties of Transition-Metal Dichalcogenides Sheets by Spontaneous Gold Nanoparticle Decoration. *The Journal of Physical Chemistry Letters* **2013**, *4* (8), 1227-1232. DOI: 10.1021/jz400507t.
(25) Lobo, K.; Gangaiah, V. K.; Priya, H.; Matte, H. S. S. R. Spontaneous formation of gold nanoparticles on MoS2 nanosheets and its impact on solution-processed optoelectronic devices. *iScience* **2022**, *25* (4), 104120. DOI: https://doi.org/10.1016/j.isci.2022.104120.
(26) Ganguly, A.; Trovato, O.; Duraisamy, S.; Benson, J.; Han, Y.; Satriano, C.; Papakonstantinou, P. Organic Solvent Based Synthesis of Gold Nanoparticle−Semiconducting 2H-MoS2 Hybrid Nanosheets. *The Journal of Physical Chemistry C* **2019**, *123* (16), 10646-10657. DOI: 10.1021/acs.jpcc.9b00303.
(27) Cho, S.-Y.; Koh, H.-J.; Yoo, H.-W.; Kim, J.-S.; Jung, H.-T. Tunable Volatile-Organic-Compound Sensor by Using Au Nanoparticle Incorporation on MoS2. *ACS Sensors* **2017**, *2* (1), 183-189. DOI: 10.1021/acssensors.6b00801.
(28) Zhang, R.; Li, Y.; Qi, J.; Gao, D. Ferromagnetism in ultrathin MoS2 nanosheets: from amorphous to crystalline. *Nanoscale research letters* **2014**, *9*, 586. DOI: 10.1186/1556-276X-9-586.
(29) Huang, S.; You, Z.; Jiang, Y.; Zhang, F.; Liu, K.; Liu, Y.; Chen, X.; Lv, Y. Fabrication of Ultrathin MoS2 Nanosheets and Application on Adsorption of Organic Pollutants and Heavy Metals. *Processes* **2020**, *8*, 504. DOI: 10.3390/pr8050504.
(30) Sivakumar, M.; Venkatakrishnan, K.; Tan, B. Characterization of MHz pulse repetition rate femtosecond laser-irradiated gold-coated silicon surfaces. *Nanoscale Research Letters* **2011**, *6* (1), 78. DOI: 10.1186/1556-276X-6-78.
(31) Baker, M. A.; Gilmore, R.; Lenardi, C.; Gissler, W. XPS investigation of preferential sputtering of S from MoS2 and determination of MoSx stoichiometry from Mo and S peak positions. *Applied Surface Science* **1999**, *150* (1), 255-262. DOI: https://doi.org/10.1016/S0169-4332(99)00253-6.
(32) Fang, H.; Tosun, M.; Seol, G.; Chang, T. C.; Takei, K.; Guo, J.; Javey, A. Degenerate n-Doping of Few-Layer Transition Metal Dichalcogenides by Potassium. *Nano Letters* **2013**, *13* (5), 1991-1995. DOI: 10.1021/nl400044m.
(33) Dunklin, J. R.; Lafargue, P.; Higgins, T. M.; Forcherio, G. T.; Benamara, M.; McEvoy, N.; Roper, D. K.; Coleman, J. N.; Vaynzof, Y.; Backes, C. Production of monolayer-rich gold-decorated 2H–WS2 nanosheets by defect engineering. *npj 2D Materials and Applications* **2018**, *1* (1), 43. DOI: 10.1038/s41699-017-0045-z.
(34) Lee, C. Y.; Strano, M. S. Understanding the Dynamics of Signal Transduction for Adsorption of Gases and Vapors on Carbon Nanotube Sensors. *Langmuir* **2005**, *21* (11), 5192-5196. DOI: 10.1021/la046867i.
(35) Eom, W.; Jang, J.-S.; Lee, S. H.; Lee, E.; Jeong, W.; Kim, I.-D.; Choi, S.-J.; Han, T. H. Effect of metal/metal oxide catalysts on graphene fiber for improved NO2 sensing. *Sensors and Actuators B: Chemical* **2021**, *344*, 130231. DOI: https://doi.org/10.1016/j.snb.2021.130231.
(36) Wu, R.; Hao, J.; Zheng, S.; Sun, Q.; Wang, T.; Zhang, D.; Zhang, H.; Wang, Y.; Zhou, X. N dopants triggered new active sites and fast charge transfer in MoS2 nanosheets for full Response-Recovery NO2 detection at room temperature. *Applied Surface Science* **2022**, *571*, 151162. DOI: https://doi.org/10.1016/j.apsusc.2021.151162.

(37) Choi, S.-J.; Kim, S.-J.; Jang, J.-S.; Lee, J.-H.; Kim, I.-D. Silver Nanowire Embedded Colorless Polyimide Heater for Wearable Chemical Sensors: Improved Reversible Reaction Kinetics of Optically Reduced Graphene Oxide. *Small* **2016**, *12* (42), 5826-5835. DOI: https://doi.org/10.1002/smll.201602230 (acccessed 2024/03/22).
(38) Choi, S.-J.; Lee, D.-M.; Yu, H.; Jang, J.-S.; Kim, M.-H.; Kang, J.-Y.; Jeong, H. S.; Kim, I.-D. All-carbon fiber-based chemical sensor: Improved reversible NO2 reaction kinetics. *Sensors and Actuators B: Chemical* **2019**, *290*, 293-301. DOI: https://doi.org/10.1016/j.snb.2019.03.134.
(39) Choi, S.-J.; Choi, H.-J.; Koo, W.-T.; Huh, D.; Lee, H.; Kim, I.-D. Metal–Organic Framework-Templated PdO-Co3O4 Nanocubes Functionalized by SWCNTs: Improved NO2 Reaction Kinetics on Flexible Heating Film. *ACS Applied Materials & Interfaces* **2017**, *9* (46), 40593-40603. DOI: 10.1021/acsami.7b11317.
(40) Lee, C. Y.; Sharma, R.; Radadia, A. D.; Masel, R. I.; Strano, M. S. On-Chip Micro Gas Chromatograph Enabled by a Noncovalently Functionalized Single-Walled Carbon Nanotube Sensor Array. *Angewandte Chemie International Edition* **2008**, *47* (27), 5018-5021. DOI: https://doi.org/10.1002/anie.200704501 (acccessed 2024/03/22).
(41) Zhang, S.-L.; Choi, H.-H.; Yue, H.-Y.; Yang, W.-C. Controlled exfoliation of molybdenum disulfide for developing thin film humidity sensor. *Current Applied Physics* **2014**, *14* (3), 264-268. DOI: https://doi.org/10.1016/j.cap.2013.11.031.
(42) Park, S. Y.; Lee, J. E.; Kim, Y. H.; Kim, J. J.; Shim, Y.-S.; Kim, S. Y.; Lee, M. H.; Jang, H. W. Room temperature humidity sensors based on rGO/MoS2 hybrid composites synthesized by hydrothermal method. *Sensors and Actuators B: Chemical* **2018**, *258*, 775-782. DOI: https://doi.org/10.1016/j.snb.2017.11.176.
(43) Sun, Y.; Hu, J.; Zhang, Y. Visible light assisted trace gaseous NO2 sensor with anti-humidity ability via LSPR enhancement effect. *Sensors and Actuators B: Chemical* **2022**, *367*, 132032. DOI: https://doi.org/10.1016/j.snb.2022.132032.
(44) Jaiswal, J.; Sanger, A.; Tiwari, P.; Chandra, R. MoS2 hybrid heterostructure thin film decorated with CdTe quantum dots for room temperature NO2 gas sensor. *Sensors and Actuators B: Chemical* **2020**, *305*, 127437. DOI: https://doi.org/10.1016/j.snb.2019.127437.
(45) Park, S.-J.; Ha, T.-J. MoS2 monolayers functionalized with gold nanoparticles using microwave absorption for FET-type NO2 gas sensors in ppb-levels. *Applied Surface Science* **2023**, *622*, 156959. DOI: https://doi.org/10.1016/j.apsusc.2023.156959.
(46) Huang, J.; Chu, J.; Wang, Z.; Zhang, J.; Yang, A.; Li, X.; Gao, C.; Huang, H.; Wang, X.; Cheng, Y.; Rong, M. Chemisorption of NO2 to MoS2 Nanostructures and its Effects for MoS2 Sensors. *ChemNanoMat* **2019**, *5* (9), 1123-1130. DOI: https://doi.org/10.1002/cnma.201900350 (acccessed 2024/03/15).
(47) Kushwaha, A.; Goel, N. Edge enriched MoS2 micro flowered structure for high performance NO2 sensor. *Sensors and Actuators B: Chemical* **2023**, *393*, 134190. DOI: https://doi.org/10.1016/j.snb.2023.134190.